Solar Radio Spikes and Type IIIb Striae Manifestations of Subsecond Electron Acceleration Triggered by a Coronal Mass Ejection

Daniel L. Clarkson[1] , Eduard P. Kontar[1] , Nicole Vilmer[2,3] , Mykola Gordovskyy[4] , Xingyao Chen[1] , and Nicolina Chrysaphi[1,2]
[1] School of Physics & Astronomy, University of Glasgow, Glasgow, G12 8QQ, UK
[2] LESIA, Observatoire de Paris, Université PSL, CNRS, Sorbonne Université, Université de Paris, 5 place Jules Janssen, F-92195 Meudon, France
[3] Station de Radioastronomie de Nançay, Observatoire de Paris, CNRS, PSL, Université d'Orléans, Nançay, France
[4] Department of Physics & Astronomy, University of Manchester, Manchester M13 9PL, UK

Abstract

Understanding electron acceleration associated with magnetic energy release at subsecond scales presents major challenges in solar physics. Solar radio spikes observed as subsecond, narrow-bandwidth bursts with $\Delta f/f \sim 10^{-3}$–10^{-2} are indicative of a subsecond evolution of the electron distribution. We present a statistical analysis of frequency- and time-resolved imaging of individual spikes and Type IIIb striae associated with a coronal mass ejection (CME). LOFAR imaging reveals that the cotemporal (<2 s) spike and striae intensity contours almost completely overlap. On average, both burst types have a similar source size with a fast expansion at millisecond scales. The radio source centroid velocities are often superluminal and independent of frequency over 30–45 MHz. The CME perturbs the field geometry, leading to increased spike emission likely due to frequent magnetic reconnection. As the field restores itself toward the prior configuration, the observed sky-plane emission locations drift to increased heights over tens of minutes. Combined with previous observations above 1 GHz, the average decay time and source size estimates follow a $\sim 1/f$ dependence over three decades in frequency, similar to radio-wave scattering predictions. Both time and spatial characteristics of the bursts between 30 and 70 MHz are consistent with radio-wave scattering with a strong anisotropy of the density fluctuation spectrum. Consequently, the site of the radio-wave emission does not correspond to the observed burst locations and implies acceleration and emission near the CME flank. The bandwidths suggest intrinsic emission source sizes $<1''$ at 30 MHz and magnetic field strengths a factor of two larger than average in events that produce decameter spikes.

Unified Astronomy Thesaurus concepts: Solar corona (1483); Solar radio emission (1522)

1. Introduction

Radio bursts are routinely emitted in the outer solar corona due to the acceleration of energetic electrons in solar flares and coronal mass ejections (CMEs). Among the many solar radio burst types, radio spikes are likely the shortest, with narrow spectral widths. They are emitted over wide frequency ranges, and have been suggested to be caused by plasma emission (e.g., Zhezezniakov & Zaitsev 1975; Chernov 1977; Melnik et al. 2014) or electron-cyclotron maser (ECM) emission (e.g., Melrose & Dulk 1982; Cliver et al. 2011; Chernov 2011) depending on the coronal conditions at the height of emission. Considering the narrow bandwidths with the plasma emission hypothesis implies that the production of Langmuir waves and stimulation of radio emission occurs over short distances that were previously suggested to be the result of weak electron beams—i.e., small spatial sizes and low beam densities (Tarnstrom & Philip 1972a; Melnik et al. 2014). Previous studies have considered spike emission resulting from electron acceleration occurring in many small sites (Benz et al. 1982) and the fragmentation of flare energy release (Benz 1985). At gigahertz frequencies, millisecond spikes are suggested to be produced via ECM emission in numerous sources due to magnetic inhomogeneities (Rozhansky et al. 2008) that could produce fragmentation secondary to that of primary energy

release (Fleishman & Mel'nikov 1998). However, it is difficult to reconcile the ECM emission model with observations below 130 MHz in post-eruption loop systems (Cliver et al. 2011) as the plasma density would be too high to satisfy the condition $f_{ce} \gtrsim f_{pe}$.

While spikes have been observed and studied over a number of decades, imaging observations are relatively sparse and were previously limited to decimeter wavelengths, relating spikes to the site of the energy release (Krucker et al. 1995, 1997; Paesold et al. 2001), near loop tops (Benz et al. 2002), and at the site of magnetic loop compression induced by a CME (Khan & Aurass 2006).

The earliest one-dimensional imaging observations of spikes at 2.8 GHz (Gary et al. 1991) have found that different spike sources are produced from the same one-dimensional location to within $0\overset{''}{.}9$ using amplitude and phase data, with a $\sim 25''$ displacement from a continuum source. Altyntsev et al. (1995, 1996) report linear source sizes up to $46''$ at 5.7 GHz, deconvolved from the instrument beam. They find the spikes to coincide spatially with an underlying microwave burst within $12''$. From two-dimensional imaging, Krucker et al. (1995) resolve only the minor axis of the emission with an observed size of $90''$ at 333 MHz. More recently, Battaglia et al. (2021) measure a FWHM size from a 2D Gaussian fit of $20''$ at 1.1 GHz, but the burst is not spatially resolved because the beam size is $60''$, and can only be considered as a lower limit. Generally, the majority of past imaging observations provide limited information of the events, without any specific detail of the individual spike source evolution in time, frequency, and

space. Clearly, improved spike imaging from high-sensitivity instruments is required.

At decameter wavelengths, the spike analysis was restricted to dynamic spectra (e.g., Barrow et al. 1994; Melnik et al. 2014; Shevchuk et al. 2016) until recent observations presented time- and frequency-resolved imaging of individual spike sources (Clarkson et al. 2021). Since radio waves are subject to significant refraction and scattering effects as they propagate through a turbulent corona, causing extended time profiles, substantially larger source sizes, and displaced positions in the plane of sky (e.g., Kontar et al. 2017b), the unprecedented resolution of the LOw Frequency ARray (LOFAR) allowed tracking of the spike source evolution at fixed frequencies over subsecond scales. The results imply that radio-wave scattering governs the time duration and peculiar motion. Further, the observed characteristics of decameter spikes are consistent with that of individual Type IIIb striae in the same event, including the same sense of polarization, suggesting a common physical mechanism in a region of space in which the magnetic field strength is not sufficient to satisfy the conditions for ECM emission. Moreover, the bursts were weakly polarized, which is contrary to the strong polarization expected from ECM emission (Melrose & Dulk 1982). The decameter spikes were therefore considered to be produced via plasma emission.

These results are consistent with simulations of radio-wave scattering (Kontar et al. 2019), which show that a degree of anisotropy α between 0.2 and 0.3 within the density fluctuation spectrum is required in order to explain observational results (Kontar et al. 2019; Chen et al. 2020; Kuznetsov et al. 2020; Musset et al. 2021), where $\alpha \equiv q_\parallel / q_\perp$ and $q_{\parallel,\perp}$ are the wavevector components of the electron density fluctuations. The simulations in Kuznetsov et al. (2020) show that sources observed away from the disk center can present superluminal centroid velocities, as was observed for striae (Zhang et al. 2020) and spikes (Clarkson et al. 2021). If the source motion is nonradial, then sources closer to the disk center can also present speeds near c, as observed by drift-pair bursts (Kuznetsov & Kontar 2019).

In this work, we present an analysis of over 1000 spikes using LOFAR, allowing a much needed statistical determination of the various spike characteristics between 30 and 45 MHz from imaging observations and 30–70 MHz from dynamic spectra, and compare with 250 individual striae of Type IIIb bursts. We analyze the centroid locations of both spikes and striae within a closed magnetic loop in conjunction with a CME, and compare the results to scattering simulations and observations over a wide frequency range within the literature.

2. Overview of the Observations

Clusters of radio spikes and Type IIIb bursts were observed by the LOFAR (van Haarlem et al. 2013) on 2017 July 15 between 10:17 and 11:39 UT, associated with a CME. Figure 1(a) shows the LASCO C2 field of view at 11:36 UT, where two narrow CME fronts, one of which is a streamer-puff CME (Bemporad et al. 2005), are observed to erupt near 10:52 UT as the result of a jet (see Chrysaphi et al. 2020, for details). Also shown is an SDO/AIA 171 Å image of the Sun at 11:21 UT, and a potential field source surface (PFSS) extrapolation showing the open and closed magnetic geometry at noon. The active region AR12665 that causes the flaring emission is located within the western solar hemisphere at a longitude of

$\theta = 52°$ and latitude $\phi = -8°$ as viewed from Earth. 1076 individually resolved spikes and 250 striae have been analyzed with 421 spikes (207 striae) at frequencies between 30 and 45 MHz. Above this frequency, significant side-lobe emission can often be brighter than the main-lobe emission and was therefore not used for imaging. Figures 1(b)-(d) shows example dynamic spectra of the spike emission. Six Type IIIb J bursts within the event are chosen for analysis, one of which is shown in Figure 1(e) with a starting frequency of 45 MHz for the fundamental, with a possible harmonic branch observed between 60 and 66 MHz correlating to the lower frequency portion of the fundamental.

The observations were designed to have tied-array beams between 30 and 70 MHz using the Low Band Antenna (LBA) stations in the outer configuration, with a maximum core baseline of ∼3.6 km. The configuration provides 217 interferometrically synthesized beams that image the solar corona up to a radius of ∼3 $R_\odot$, with a maximum temporal and spectral resolution of 10 ms and 12.2 kHz, respectively (see Kontar et al. 2017b, for details). To minimize noise, the data were reduced temporally to 20 ms resolution. During the observation, a single beam at the northern outer edge of the mosaic pattern across the solar disk recorded no data, and was discarded during analysis. The beam intensities are interpolated on a regular grid to produce the radio images. Observations of Tau A were used to calibrate the flux (e.g., Kontar et al. 2017b) to solar flux units (sfu; 1 sfu = 10^{-22} W m^{-2} Hz^{-1}).

Spike and striae characteristics are measured from both dynamic spectra and imaging observations as in Clarkson et al. (2021). Specifically, the radio source (see Figure 7 for an example) that is convolved with the LOFAR point-spread function (PSF) is well approximated by a 2D elliptical Gaussian that dictates the centroid position x_c, y_c of the observed sources. The peak time is defined at the central index of the flux profile within 15% of the maximum, with the rise and decay position at the start and end of the FWHM duration. Ionospheric refraction can cause a noticeable shift in the observed radio emission dependent on the source elevation. We correct all centroid positions with respect to the zenith angle at $z = 32°.4$ for average ionospheric conditions as in Gordovskyy et al. (2022; see Equation (6)).

3. Acceleration Region

3.1. Type IIIb Bidirectional Exciter Motion

The Type IIIb bursts provide a useful diagnostic of the coronal loop that their sources trace partially. The example shown in Figures 1(e) and 2(a) has a negative bulk drift of -6.1 MHz s^{-1} near 40 MHz, comparative to previously reported Type IIIb drift rates (Chen et al. 2018; Sharykin et al. 2018), and reduces to -1.1 MHz s^{-1} at 32 MHz as the exciter approaches the loop apex, similar to other decameter J bursts (Reid & Kontar 2017). Above these frequencies, the burst exhibits a reverse drift at 4.9 MHz s^{-1}, signifying electrons that are propagating toward the footpoints. Figure 2 shows the peak centroid locations for the J burst as a function of time, separated by the bulk drift direction. The bidirectional burst exciter motion (Aschwanden et al. 1995; Tan et al. 2016) suggests that the acceleration region of the Type IIIb burst is at a radius corresponding to ∼40 MHz where the opposing centroid motions (bulk drifts) emanate, implying that in
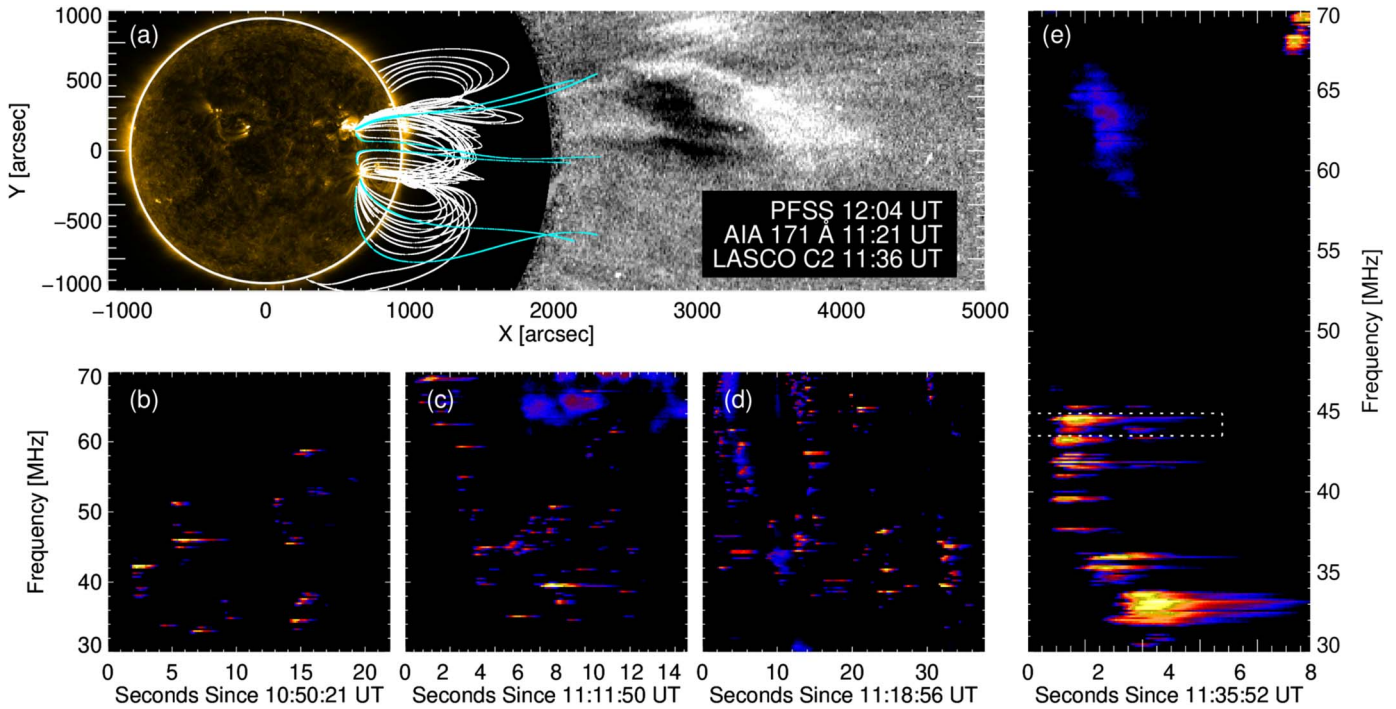
Figure 1. An overview of the event. Panel (a) SDO/AIA 171 Å image at 11:20:57 UT, superimposed with a PFSS extrapolation at noon showing both open (blue) and closed (white) field lines within the region surrounding the active region and northern sunspot, and a LASCO C2 image showing the streamer-puff (above) and narrow (below) CME fronts at 11:36:05 UT, as shown in Chrysaphi et al. (2020). Panels (b-d) Dynamic spectra showing samples of the spike emission. Panel (e) Dynamic spectra of a Type IIIb J burst. The dotted box highlights the region shown in Figure 7. All dynamic spectra are background subtracted, where the background is defined using a region at the start of each dynamic spectrum containing no bursts at all frequencies.

general, the site of acceleration for this event is high in the corona.

3.2. Inferred Loop Density Model

Figure 2(b) displays the frequency position according to an exponential loop density model (e.g., Aschwanden et al. 1999), given by

$$n_e(l) = A_n \exp\left(-\frac{r(l)}{r_n}\right), \qquad (1)$$

where $A_n = 10^{11}$ cm^{-3}, $r_n = 1.57 \times 10^{10}$ cm is the density scale height similar to values found by Reid & Kontar (2017) for Type III U and J bursts, and $r(l)$ is the height along the loop from the solar surface. The angle formed between the latitude and longitude of each active region to solar north is $\Phi \sim -27°$. The density model is then rotated around the x- and y-axes as

$$\begin{aligned} x' &= x \cos\theta \\ y' &= y \cos\Phi + x \sin\theta \sin\Phi, \end{aligned} \qquad (2)$$

which produces the dashed lines representing the frequencies of the density model. The value of r_n was then chosen to best represent the centroid locations at a given frequency. The inset of Figure 2(b) displays the applied rotation.

3.3. Type IIIb Beam Velocities

The centroid positions of the reverse-slope component of the Type IIIb J burst are distributed across $80''\!.6 \pm 11''$ of the sky plane over 0.9 s. The distance uncertainty is derived from

the average centroid uncertainties $\overline{\delta x_c}$, $\overline{\delta y_c}$ as $\delta r = [(\partial r/\partial x \overline{\delta x_c})^2 + (\partial r/\partial y \overline{\delta y_c})^2]^{1/2}$. This correlates to a beam velocity of $v_{\rm rev,obs} = (0.22 \pm 0.03)c$. For the negative drift component, the observed radial spread is $103''\!.0 \pm 9''$ over 3 s, giving $v_{\rm obs} = (0.07 \pm 0.02)c$. Due to the projection effect, these observed values are likely to be higher. The actual velocities can be estimated as $v_{\rm obs}/\sin 52°$ assuming that the sources propagate along the plane connecting the Sun center and active region. The uncertainty in this velocity is increased because we do not know the spread in angle that the magnetic field geometry makes with the active region. Here we assume a spread of 30°. The projection-corrected beam velocities are then $v_{\rm corr} = (0.09 \pm 0.03)c$ and $v_{\rm rev,corr} = (0.28 \pm 0.06)c$. The beam velocities can also be estimated via the assumption of a density model (Equation (1)). Panels (c-d) of Figure 2 show the distance-time spectra of each burst component where the striae peaks are fit with a linear model. The gradient then provides the beam velocity through space as $(0.07 \pm 0.04)c$ and $(0.27 \pm 0.02)c$ for the normal and reverse-drifting components, respectively. While each method to determine the beam velocity requires some assumption (projection effect or density model), the determined velocities agree within their errors.

3.4. Acceleration Site Location

Figure 3 shows the observed spike and striae centroid heights in the sky plane as a function of frequency and time. For the bursts pre-CME, the heights vary linearly with frequency between 30 and 45 MHz. After the onset of the flare and passage of the CME, the heights at a given frequency are reduced. In panel 2, the variation with frequency is minimal and then progressively increases over ~45 minutes. The increase in the observed sky-plane height at 30 MHz over time
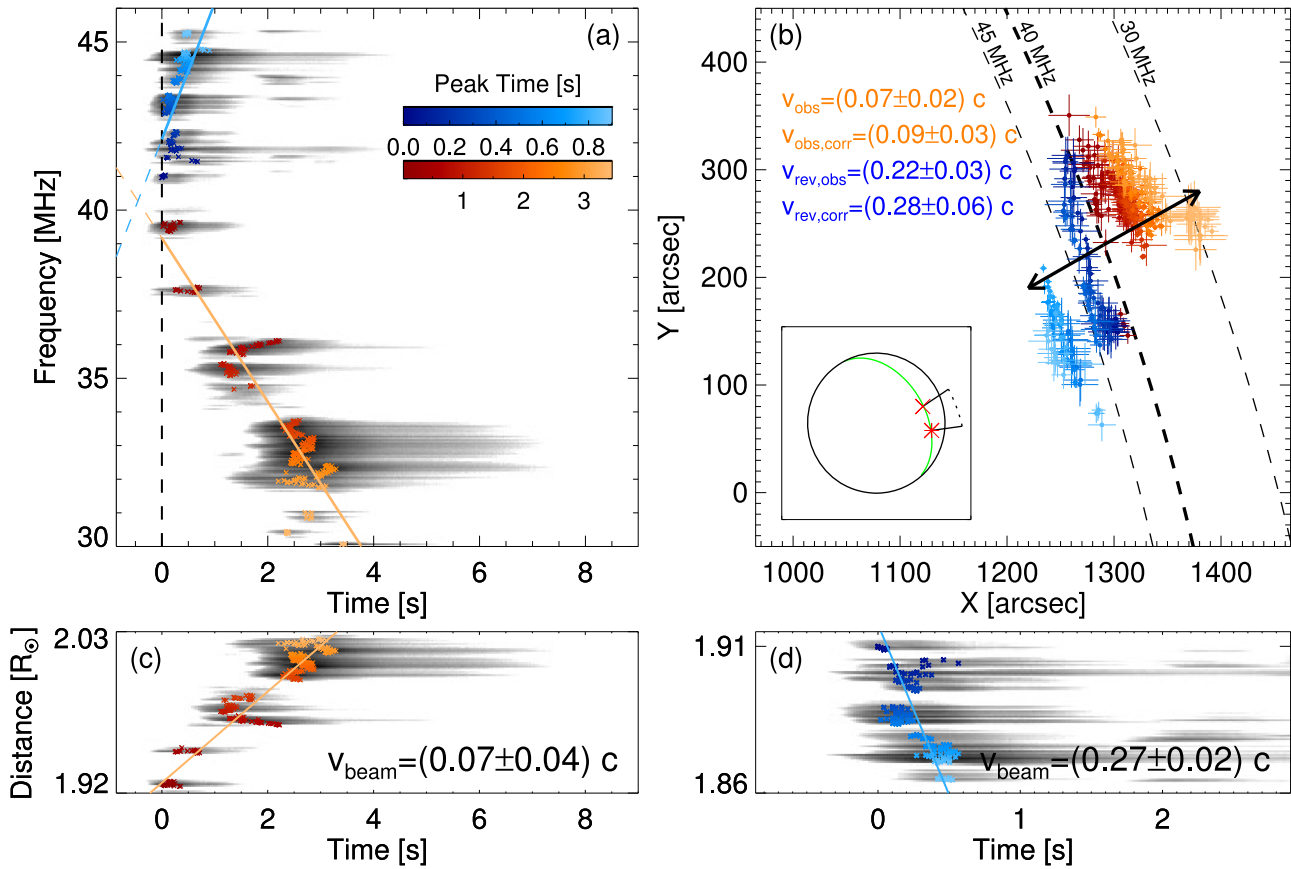
Figure 2. Centroid positions at the striae peaks of the Type IIIb J burst, marked by the colored points in the dynamic spectrum of panel (a). The orange and blue lines in panel (a) highlight the opposite-sign bulk drift rates. In all panels, the orange points relate to the negative drifting burst segment, and the blue points relate to the reverse-drifting section. The color gradients show the elapsed time from the earliest striae peak, represented by the vertical dashed black line in panel (a). Panel (b) shows the centroid locations of each striae, with the arrows representing the observed trajectories and radial distances used to estimate the centroid velocities v_{obs}, v_{rev} of each component across the plane of sky. A velocity estimate with a correction for the projection effect is given as $v_{\mathrm{obs,corr}}$ and $v_{\mathrm{rev,corr}}$ assuming the sources propagate along the Sun center and active region plane with an uncertainty corresponding to a magnetic field spread of 30°. The dashed black curves show the exponential loop density model of Equation (1) rotated as demonstrated in the inset of panel (b). Panels (c) and (d) show the distance-time spectra of each burst component with the distance obtained from the density model of Equation (1). The gradient of the linear fits to the striae peaks provides the beam velocities.
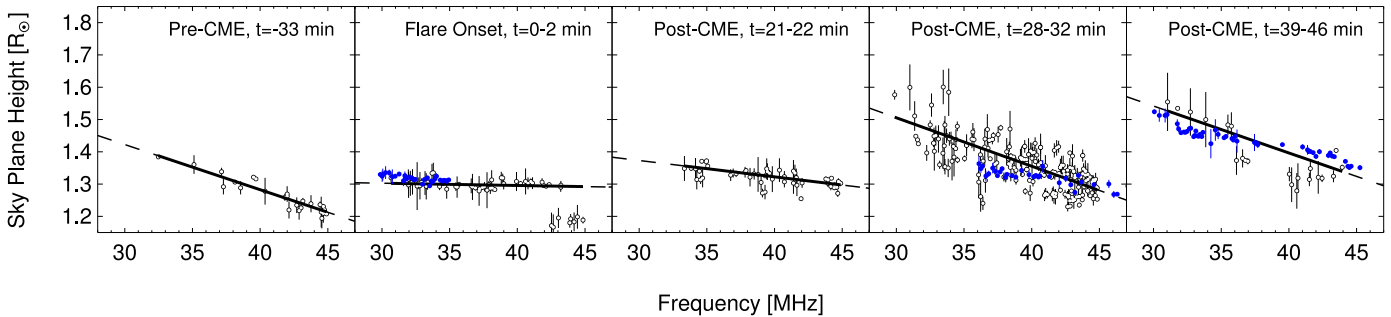

Figure 3. Observed centroid radial heights with frequency in the sky plane for spikes (open black circles) and striae (closed blue circles). Each panel shows bursts that are close in time, with the second panel near the time of the flare, such that the prior panel shows pre-CME spikes. The spike data are fit with linear models.

is shown in Figure 4 from 1.30 to 1.54 $R_{\odot}$. The variation is linear, and correlates to a velocity of $v_{\mathrm{H,obs}} = (81 \pm 5)\,\mathrm{km\,s^{-1}}$. The actual radial heights can be estimated by correcting for the projection effect as presented in Section 3.3, leading to a corrected velocity of $v_{\mathrm{H,corr}} = (90.2 \pm 24)\,\mathrm{km\,s^{-1}}$.

4. Observed Characteristics

4.1. Comparison of Spike and Striae Centroid Positions

The centroid position of both spikes and striae differs greatly depending on the point in time that is used to generate the radio

image. Figure 5 shows the centroid motion across the FWHM of the time profile of individual striae from the Type IIIb at various fixed frequencies. There are two visible components of motion—a frequency drift away from the Sun associated with the path of the exciter, and a displacement over time at fixed frequencies almost parallel to the solar limb toward solar north, which is typically increased during the decay phase compared to the rise phase. We note that while the frequency drift and exciter trajectory do not correlate to the local field line direction of an inferred coronal loop, it implies that the actual emitter location is farther down the loop leg in a region in which the
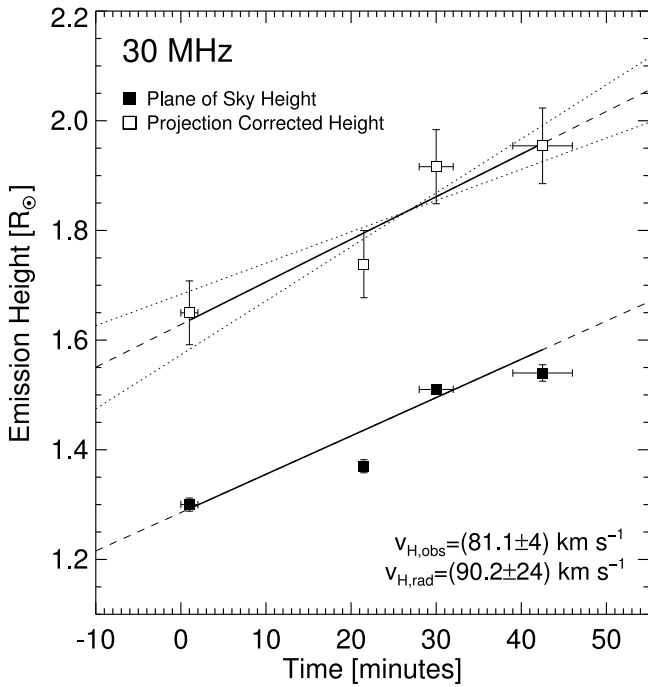
Figure 4. Observed sky-plane heights (solid squares) and estimated radial heights of the spike bursts over time at 30 MHz extrapolated from the linear fits in Figure 3. The horizontal error denotes the width of the time interval in each panel of Figure 3. The vertical error of the plane-of-sky heights is derived from the linear fits in Figure 3. The projection-corrected heights assume a spread in angle of the loop magnetic field of 30°, contributing to the increased uncertainty. These data are fit with a linear model (solid lines) where the gradient describes the velocity at which the emission height at 30 MHz increases over time. The dotted lines demonstrate the fit uncertainty for the projection-corrected heights.
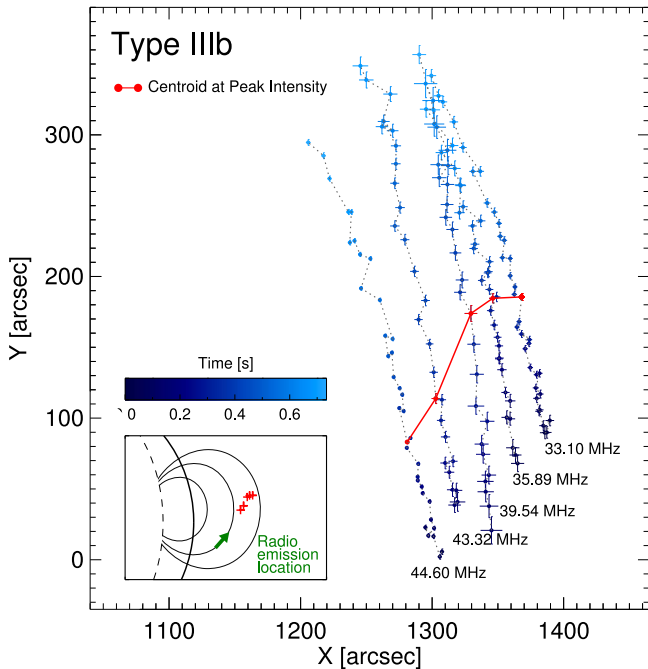
Figure 5. Type IIIb J-burst centroid locations of individual striae throughout the FWHM of the time profile at fixed frequencies. The red points and connected line represent the centroid at the peak intensity of each striae. The inset depicts coronal loop field lines with the likely location and path of the radio source (green arrow) corresponding to where the peak trajectory matches the field line direction. The red pluses mark the locations of the peak centroid.

field line trajectory matches the observed frequency drift direction, as indicated by the green arrow in the inset of Figure 5.

The fixed-frequency centroid motion evolution of the spikes across the FWHM time duration is shown in Figure 6. The individual and collective motion exhibits a displacement trajectory consistent with that shown by the striae, correlating in position with the closed magnetic field lines implied from the PFSS extrapolation. At a given frequency between 40 and 45 MHz, the spikes and striae centroids appear to drift linearly, but at lower frequencies, their motion is curved.

Figure 7 compares an individual spike and striae separated by 1.82 s and 207 kHz. The contours represent the intensity of the radio main lobes, overlaid on the apparent images of the spike emission. The burst contours are aligned in time at their respective peaks, and each panel shows the contour locations in intervals of 0.2 s before and after the peak. During the rise phase, the 90% contour levels overlap almost entirely with the average peak intensity locations above the 90% level separated by tens of arcseconds. At the 50% level, the spike contours are varied in shape compared to the striae toward the top left corner of the image. This is likely a secondary lobe of the PSF (see Figure 6(d) in Gordovskyy et al. 2022) and the lower intensity of the spike emission. During the decay phase, the contours are shifted vertically and rotated toward the limb by a similar angle, and the intensity peaks become separated. The shifted distance shown here is greater than that displayed in Figures 5 and 6 as the latter only show the FWHM period.

4.2. Spike Centroid Velocity, Source Area, and Expansion

From the observed centroid motion in time at fixed frequencies, the spike plane-of-sky centroid velocity can be measured as $v = \sqrt{v_x^2 + v_y^2}$, where $v_x = dx_c/dt$ is obtained from linear fits to the x centroid position over time, and similarly for v_y. The velocities are often superluminal with an average of $1.27c$ (Figure 8). The measured centroid velocities from radio-wave scattering simulations (Kontar et al. 2019; Kuznetsov et al. 2020) are consistent with the median observed spike velocities, and both data sets show no frequency dependence between 30 and 45 MHz.

The area of the radio source is measured at the FWHM level given by $A = (\pi/4)S_{maj}S_{min}$, where S_{maj} and S_{min} are the FWHM major and minor axis sizes of the fitted ellipse. The errors are estimated as in Kontar et al. (2017b). At 30 MHz, the angular resolution of LOFAR is ∼9′, and the beam size at the time of observation is 115 arcmin^2, reducing to 64 arcmin^2 at 45 MHz. The areal and linear expansion rates are given by fitting the change in area and ellipse axe widths over time with a linear model. Individual spike characteristics measured from imaging are shown in the Appendix (Figure A1).

4.3. Temporal and Spectral Spike Profiles

The light curve of each spike was analyzed at the central frequency f_c. The variation between individual burst time profiles causes ambiguity when all bursts are approximated with a single model, so we measure the rise τ_r and decay τ_d times directly from the data between the first point above the half-maximum level to the peak (τ_r) and from the peak to the final value above the half-maximum level (τ_d). The FWHM spike duration is then $\tau = \tau_r + \tau_d$ (Guedel & Benz 1990;
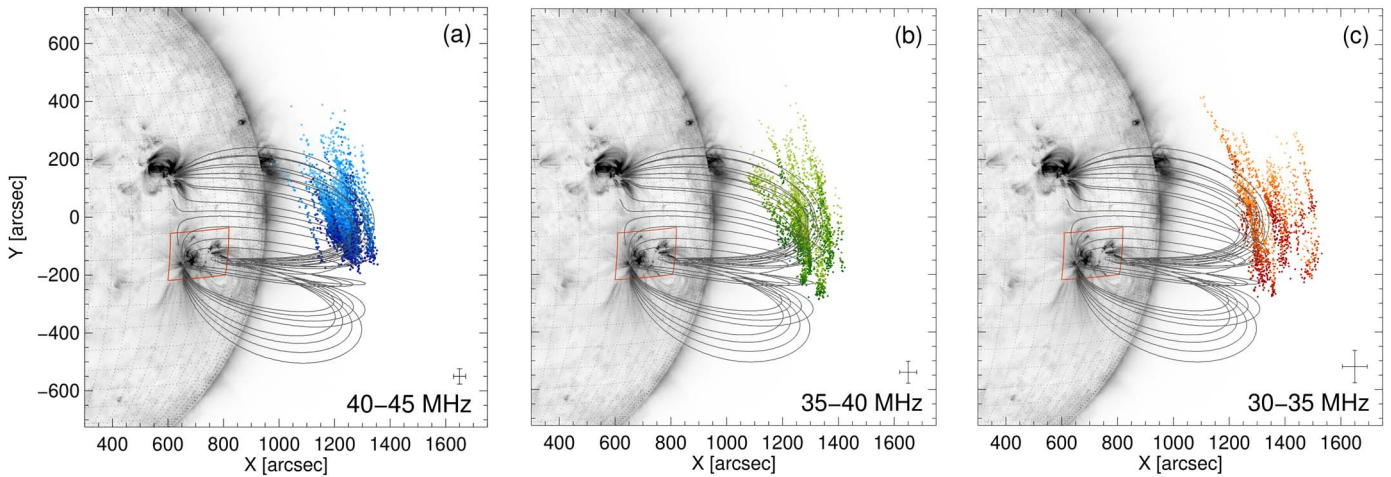
Clarkson et al.

Figure 6. Centroid positions of post-CME spikes across the FWHM intensity. Each individual spike is measured along its central frequency, with the collective motion grouped between (a) 40–45 MHz, (b) 35–40 MHz, and (c) 30–35 MHz, and overlaid on an SDO/AIA image at 171 Å. The color gradients represent time increasing from dark to light. The average centroid error within each frequency band is indicated in the bottom right corner of each panel. The thin gray lines show the closed magnetic field lines from a PFSS extrapolation. The red box on the solar surface bounds the active region.
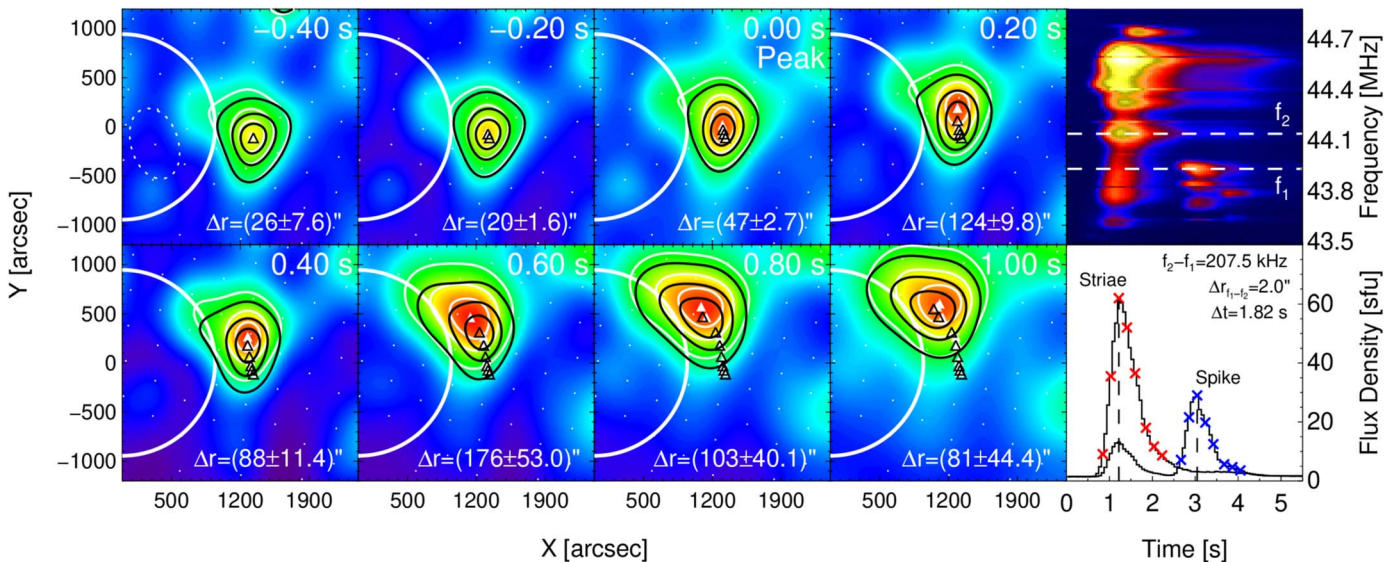
Figure 7. Comparison of spike and striae image contours with time. The left panels display the contours of spike (white) and striae (black) emission from bursts at 44 MHz that have a peak flux 1.82 s apart, overlaid on the spike images with the background (average intensity of the faintest 10 beams) subtracted. The contour levels are given at 90, 75, and 50% of the maximum image flux. The peak of the each burst is set to $t = 0.0$ s, with each panel showing the image at intervals of 0.2 s before or after the peak. The triangles track the motion of the spike (filled white) and striae (black) main lobes, with each symbol marking the average position of the image peak within 10% of the maximum flux at each time. The separation distance of the peak locations in each panel is given by Δr, with the uncertainty given as $\delta r = \Delta r [(\Delta x_{\rm err}/\Delta x)^2 + (\Delta y_{\rm err}/\Delta y)^2]^{1/2}$, where $\Delta x_{\rm err}, \Delta y_{\rm err} \propto \delta I/I_0$, and the peak intensity I_0 uncertainty is $\delta I \sim 1$ sfu. The white dots show the LOFAR beam locations, and the dotted oval in the first panel represents the beam size. The right two panels show the dynamic spectrum with the time profiles of the striae and spike sources along the dashed white lines. The red and blue crosses mark the time positions correlating to the images. $\Delta r_{\rm f_1-f_2}$ represents the distance in space between $\sim$200 kHz according to the density model of Equation (1).

Barrow et al. 1994; Reid & Kontar 2018a). The uncertainty on the rise and decay times is a combination of the background ($\sim$1 sfu at 30 MHz, increasing to 3–4 sfu at 70 MHz) and flux uncertainty, which is typically $\sim$1 sfu.

The drift rate of each spike across the FWHM duration was calculated by fitting the frequency-flux profile at each time index with a Gaussian and fitting the position in time and frequency of each Gaussian peak with a linear model where the gradient provides the spike frequency drift rate (see Clarkson et al. 2021, for an example). For this event, the spike drift rates are a few dozen kilohertz per second, with a weak tendency to increase with frequency.

The spectral shapes of the spikes are symmetrical and well approximated by a Gaussian of the form $I = I_0 \exp[-(f - f_c)^2/2\sigma^2] + I_{\rm bg}$, where $I_{\rm bg}$ gives the background intensity, and σ is the standard deviation. The FWHM spectral bandwidth is given by $\Delta f = \sigma \cdot 2\sqrt{2 \ln 2}$. Figure 9 shows the histogram of the spike bandwidth ratios within this event. The distribution is asymmetrical, with a peak near 0.1% followed by a tail that extends up to 0.6%. The peak is similar to that reported by Melnik et al. (2014) between 0.2% and 0.3% at 20–30 MHz, but lower than the gigahertz observations by Rozhansky et al. (2008) at 0.7%, although this latter value is decreased to 0.5% by Nita et al. (2008) using an updated spike
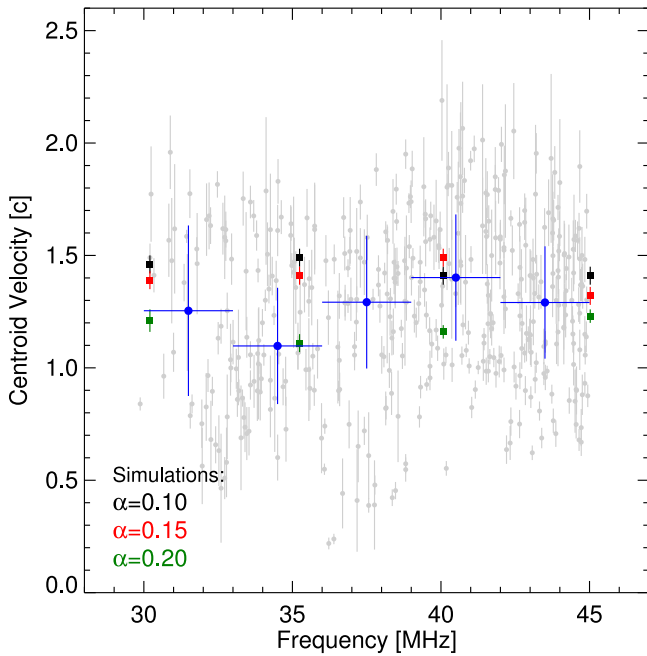
Figure 8. Spike plane-of-sky centroid velocities. The light gray points show the data with associated uncertainties. The blue points show the median values across 3 MHz bins, and the vertical error as the interquartile range represents the 25th and 75th percentiles. The squares show the centroid velocity calculated from scattering simulations of an initial point-source injection located at $\theta = 52°$, anisotropy of the density fluctuation spectrum between $\alpha = 0.1$ and 0.2, and a density fluctuation variance of $\epsilon = 0.8$.

Figure 10. Observed source sizes of spikes. The blue and red points show the median major and minor axis FWHM sizes observed by LOFAR from Figure A1(b,c). Krucker et al. (1995) observed half-maximum contour sizes of $110''$ (major) and $90''$ (minor), but the instrument beam is $112''$ (major) and $59''$ (minor), such that the source is resolved only along the minor axis—here we plot the minor axis size alone, with the error showing the upper and lower sizes of the instrument beam. Battaglia et al. (2021) note that the bursts are not spatially resolved, such that the FWHM of the fitted two-dimensional Gaussian is a lower limit. The error presented here shows the instrument beam size.

lowest bandwidth ratios, while the trends differ above $\Delta f/f \approx 0.0035$, potentially because overlapping striae broaden the measured bandwidth at lower frequencies.

Individual spike characteristics measured from dynamic spectra are shown in the Appendix (Figure A2). We note that some characteristic averages oscillate with a frequency that correlates with an oscillation in the observed flux from Tau A (Figure A2(a)). Therefore, we regard this as an instrumental artifact and not as the result of a physical solar process.

5. Comparison of Decameter and Decimeter Spike Observations

5.1. Image Sizes

The limited image measurements from previous studies (Krucker et al. 1995; Battaglia et al. 2021) are compared with the median linear spike sizes observed by LOFAR in Figure 10. The trend is consistent between each frequency range, although the decimeter measurements are not resolved along the major axes. The LOFAR-obtained major axis sizes range from $19'.5$ at 30 MHz to $13'$ at 45 MHz, decreasing as $f^{-0.98\pm0.2}$. The minor axis sizes are ~ 0.8 times the major axis, decreasing as $f^{-0.83\pm0.1}$.

5.2. Decay Times

Figure 11 combines spike average $1/e$ decay time measurements from several authors (McKim Malville et al. 1967; Guedel & Benz 1990; Barrow et al. 1994; Mészárosová et al. 2003; Shevchuk et al. 2016) between 25 MHz and 1.42 GHz.

Figure 9. Histogram of the spike (blue) and striae (black) bandwidth ratio $\Delta f/f$ distributions with a bin size of 0.05%. The bin errors are given as $\delta N = N(\sum_i \delta f_i^2 / \sum_i \Delta f_i^2)^{0.5}$, where N is the bin count, and δf is the error on the measured bandwidth. The vertical dashed lines show the LOFAR frequency resolution (12.2 kHz) at 30 and 70 MHz.

deconvolution technique. Both aforementioned distributions at gigahertz frequencies extend up to 3%, a factor of five above that observed by LOFAR in this study, perhaps because the employed algorithms can deconvolve overlapping spikes with larger bandwidths, or because of differing emission mechanisms. Figure 9 also includes the bandwidth ratio for individual striae that share a similar peak and spread to the spikes in this event. The slopes of the two distributions are comparable at the
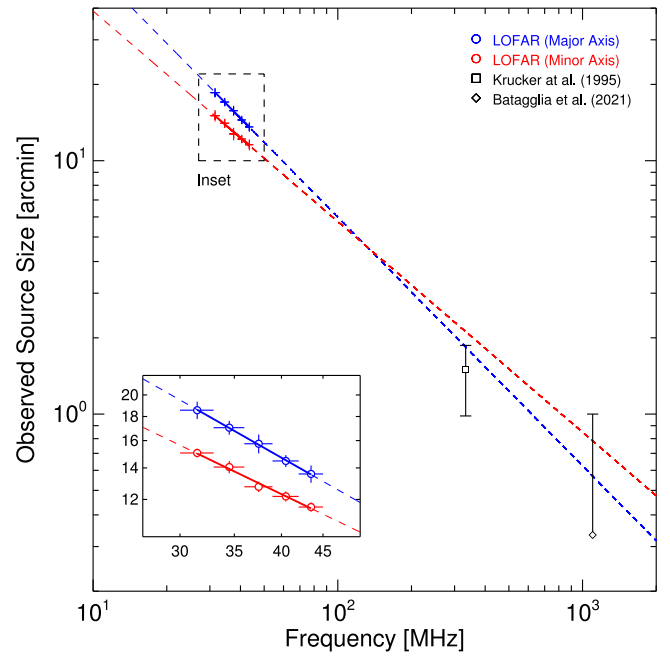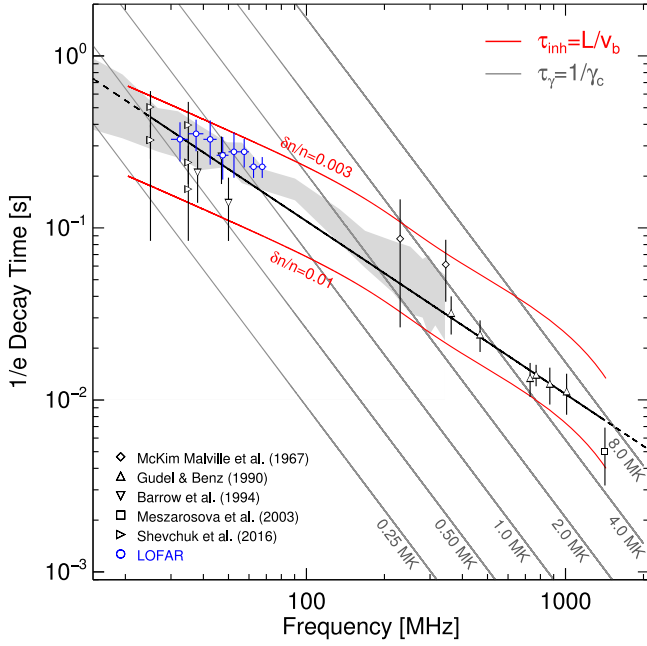
Figure 11. Average spike $1/e$ decay times against frequency. LOFAR data show the median from Figure A2(c) adjusted for the FWHM by a factor of $\sqrt{\ln 2}$. The solid black line represents the power-law fit to the data given by Equation (3). The dash–dotted gray lines represent the plasma collision time for various coronal temperatures. The gray region shows the scattering decay time for $\alpha = 0.2$ between $\epsilon = 0.5$ (lower bound) and 2.0 (upper bound). The red curves show the inhomogeneity time as defined by Equation (5) for fixed values of $\delta n/n$, as shown. For each curve, the inhomogeneity scale varies from 2 km at 1.03 $R_\odot$ to 100 km at 2 $R_\odot$.

The linear fit in log-space indicates a $1/f$ dependence as

$$\tau_d(f) = (11.22 \pm 1.9)f^{(-1.01 \pm 0.03)} \text{ s}, \ \ 25 \leqslant f \leqslant 1420 \text{ MHz}. \tag{3}$$

We include the collisional damping time given as $\tau_\gamma = 1/\gamma_c$ for various coronal temperatures T_e, where

$$\gamma_c = \pi n e^4 z_p^2 \ln\Lambda / (m_e^2 v_{Te}^3), \tag{4}$$

as defined in Reid et al. (2011), but with an additional term $z_p = 1.18$ giving the average atomic number in the photosphere (Jeffrey & Kontar 2011), and with the Coulomb logarithm $\ln\Lambda \approx 23$ (Holman et al. 2011). The density is derived from the frequency as $n = (f[\text{MHz}]/8.93 \times 10^{-3})^2$, and the parameters e, m_e, and v_{Te} are the electron charge and mass, and thermal velocity, respectively.

We also show the inhomogeneity time (e.g., Kontar 2001) as

$$\tau = \frac{|L|}{v_b} = \frac{2n_e(r)}{v_b}\left(\frac{dn_e(r)}{dr}\right)^{-1} = \frac{2n_e(r)}{v_b}\frac{\lambda}{\delta n_e}. \tag{5}$$

Here we use the density profile $n(r)$ presented in Kontar et al. (2019) with an additional term $n_c(r) = n_0 \exp(-(r-1)/h_0) + n_1 \exp(-(r-1)/h_1)$ that accounts for the sharp increase in density toward the chromosphere, where $n_0 = 1.17 \times 10^{17}$ cm^{-3} gives the density at the solar surface with $h_0 = 144$ km, providing the density scale height (Kontar et al. 2008), $n_1 = 10^{11}$ cm^{-3}, and $h_1 = 0.02$ km (e.g., Battaglia &

Kontar 2012). The final density is then $n_e(r) = n(r) + n_c(r)$. We set the beam velocity to $v_b = 10^{10}$ cm s^{-1}, and choose the scale λ to vary linearly from 2 km at 1.03 $R_\odot$ ($f_{pe} = 1.4$ GHz) to 100 km at 2 $R_\odot$ ($f_{pe} = 20$ MHz), with fixed density fluctuation amplitudes of $\delta n_e/n_e = 0.003$ and 0.01. This gives $|L| \sim (0.04–2) \times 10^4$ km when $\delta n_e/n_e = 0.01$ and $|L| \sim (0.1–6) \times 10^4$ km when $\delta n_e/n_e = 0.003$, where the upper values of $|L|$ are similar to the value considered by Kontar (2001) for electron beam dynamics with a fluctuating background density.

5.3. Bandwidth

Combined average spike bandwidth observations as a function of frequency are shown in Figure 12 (Markeev & Chernov 1971; Tarnstrom & Philip 1972b; Benz et al. 1982; Benz 1985; Staehli & Magun 1986; Benz et al. 1992; Csillaghy & Benz 1993; Benz et al. 1996; Wang et al. 1999; Messmer & Benz 2000; Wang et al. 2002; Rozhansky et al. 2008; Nita et al. 2008; Wang et al. 2008; Dábrowski et al. 2011; Melnik et al. 2014; Shevchuk et al. 2016; Tan et al. 2019) from 10 MHz to 8 GHz. Despite the possibility of over estimated average bandwidths at the higher frequencies due to limited spectral resolutions, the increase in $\Delta f/f$ above 200 MHz is expected via consideration of the Langmuir-wave dispersion relation in a weakly magnetized plasma (Melrose 1985; Pécseli 2012; Melnik et al. 2014; Shevchuk et al. 2016) as

$$\omega = \omega_{pe} + \frac{3k^2v_{Te}^2}{2\omega_{pe}} + \frac{\omega_{ce}^2}{2\omega_{pe}}\sin^2\psi, \tag{6}$$

where ψ is the angle between the plasma wave direction and the magnetic field, and $\omega_{ce} = eB/m_e c$ is the electron-cyclotron frequency. Equation (6) is valid under the condition that $\omega_{ce} \ll \omega_{pe}$ for electron beams, where the spatial size is $<10^8$ cm (Melnik et al. 2014). Figure 12 shows the expected bandwidth $\Delta\omega = \omega(\psi) - \omega(0)$ for varied magnetic field strengths based on the model by Gary (2001; see Equation (2)), with the term B_f varied between 100 and 800 G shown in panel (b) and the density model given by $n_e(r)$, shown in panel (c). A value of $B_f = 500$ G gives a magnetic field strength of $\sim$300 G at a height of 0.02 $R_\odot$ from the solar surface, as estimated by Kontar et al. (2017a). We choose $\psi = 23°$ to provide the best match to the low-frequency spike population trend when $B_f = 100$ G, similar to the angle of 20° by Zaitsev (1975) for Type III bursts.

6. Discussion

We investigated 1076 solar radio spikes to statistically retrieve their characteristics in the decameter range, and compared their centroid locations with individual Type IIIb striae within the coronal loop structure. The apparent radio map contours of each burst type that are close in time (less than a few seconds) and frequency overlap with little variation in position and shape, with any clear separation occurring during the decay phase. Both burst types experience comparable and significant displacement along the loop direction at fixed frequencies with substantial broadening over time, predominantly along the major axis.
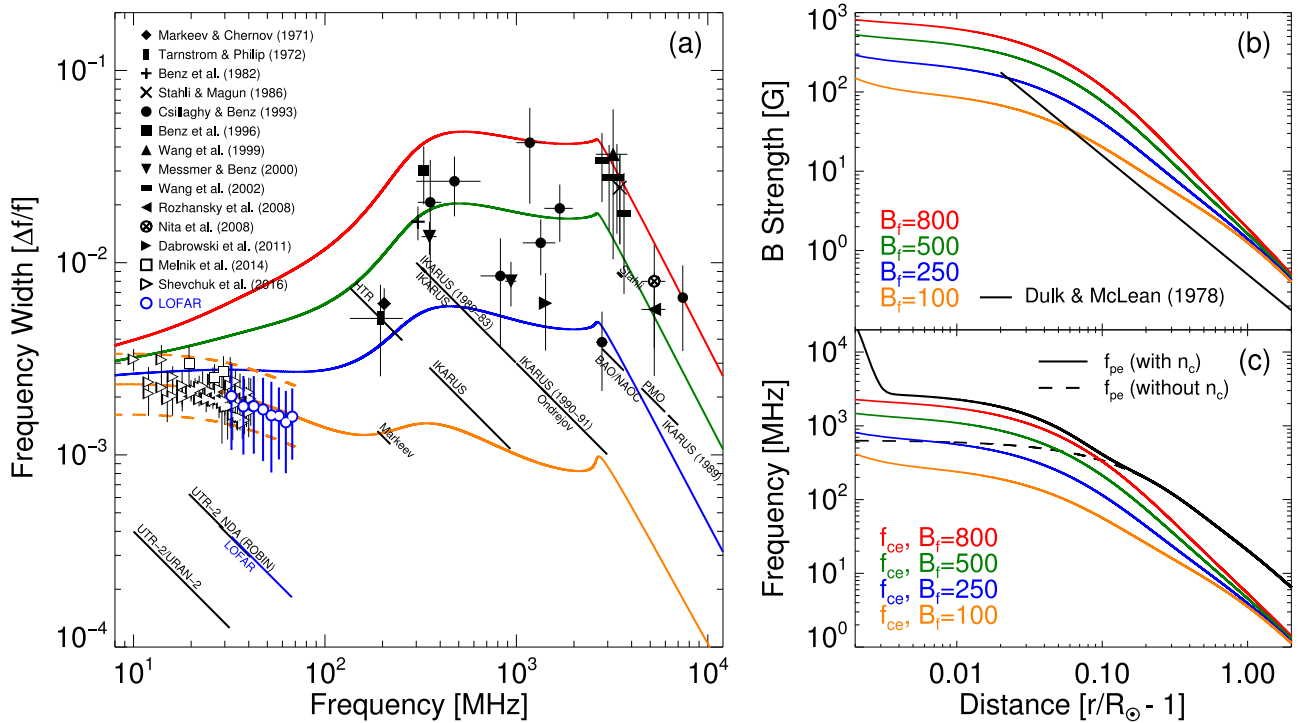
Figure 12. Panel (a) Average spike bandwidth ratio $\Delta f/f$ (where Δf is given at the FWHM level) against frequency combining observations as indicated in the legend. LOFAR data show the median from Figure A2(d). The diagonal lines represent the instrument resolutions. The colored curves denote the bandwidth derived from the Langmuir-wave dispersion relation in a magnetized plasma (Equation (6)) with $\psi = 23°$. Each color uses the magnetic field model of Gary (2001) with the constant B_f varied. The dashed orange curves vary ψ from 19° (lower) to 28° (upper). Panel (b) Magnetic field models with distance. We also show the magnetic field model from Dulk & McLean (1978) as $B(r) = 0.5(r/R_\odot - 1)^{-1.5}$. Panel (c) The plasma and cyclotron frequencies from the density and magnetic field models.

6.1. Beam Velocities and Emission Heights

From the Type IIIb bulk frequency drift, the electron beam velocity can be estimated. The reverse-slope component corresponds to a beam velocity of $0.3c$, while the outward propagating beams has a velocity of $0.1c$, which could indicate an asymmetry in the energy injected in each direction. Pre-CME, the spikes show an increase in height with decreasing frequency. After the CME ejection at approximately 10:52 UT (indicated by the Type III burst onset; Clarkson et al. 2021; and jet; Chrysaphi et al. 2020), the observed spike and Type IIIb striae heights vary weakly with frequency, which might be caused by the magnetic field being distorted such that the density gradient and loop trajectory is along the line of sight. The loop may then restore over tens of minutes toward the prior configuration with a velocity of $\sim90\,\mathrm{km\,s^{-1}}$. Interestingly, the bursts near 45 MHz seem to retain an approximately constant height, while those toward 30 MHz experience the bulk of the shift, which implies that the bulk of the rotation and/or expansion of the magnetic field occurs at the lower frequencies toward the loop top.

6.2. Anisotropic Scattering

The spike and striae centroids present two components of motion: an exciter-driven frequency-dependent radial motion, and a shift perpendicular to the radial direction over time at fixed frequencies. The latter is assumed to be independent of the exciter motion because variations in the ambient density or magnetic field will be stable over time periods of 0.1–0.5 s. We attribute the fixed-frequency displacement to radio-wave scattering in an anisotropic turbulent medium, which has previously been shown to produce such motion along the

direction of the magnetic field (Kontar et al. 2017b; Kuznetsov et al. 2020). The centroid locations can then provide insight into the magnetic field structure: above 40 MHz, the displacement is linear, becoming arced toward the limb at lower frequencies, such that the field structure may have greater curvature farther from the Sun.

We show that the median fixed-frequency centroid velocities present no frequency dependence between 30 and 45 MHz, and are replicated with radio-wave scattering simulations using strong levels of anisotropy ($\alpha = 0.1–0.2$). While varying the anisotropy factor causes a small change in the centroid velocity, the main influence is the magnetic field angle to the observer—for a field aligned perpendicularly to the observer's line of sight, the observed centroid velocity will be highest. The spread in observed velocities at a given frequency for spikes at different times suggests that the source locations are distributed across a range of angles within the loop, and that the anisotropy and turbulence levels may fluctuate over time.

6.3. Event Interpretation

Our interpretation of the event is shown in Figure 13. Beam acceleration most likely occurs along the ascending loop leg toward the lower flank of the CME, in a region closer to the Sun, in which the magnetic field geometry has a radial trajectory, inferred from the frequency drift in Figure 5. Interestingly, the Type II observed during this event is suggested to have occurred toward the opposite CME flank (Chrysaphi et al. 2020). The passage of the CME perturbs the magnetic geometry, rotating the loops toward the observer, causing any frequency dependence of emission to be masked in the sky plane. Post-CME, repeated magnetic reconnection and
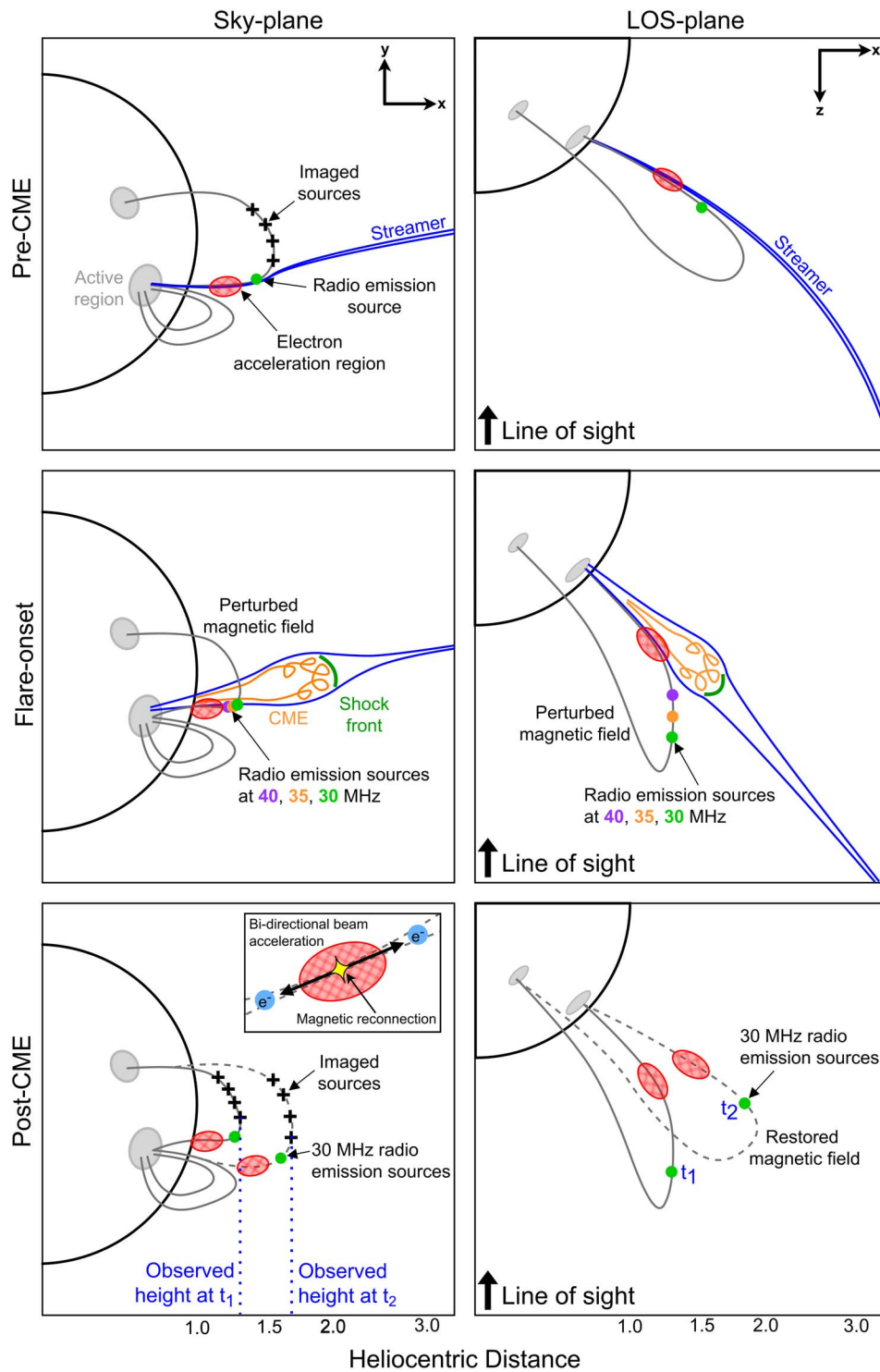
Figure 13. A cartoon of the event before and after the CME eruption. The two columns show the *x, y* sky-plane and *z, x* line-of-sight planes, respectively, with each column showing the configuration pre-CME, during the flaring period, and post-CME. Pre-CME, fewer spikes are observed, with source emission locations (colored circles) and electron acceleration (hatched red regions) likely occurring along the lower loop leg via magnetic reconnection interaction between the loops (gray lines) and streamer (blue lines). At the onset of the flare and eruption of the streamer-puff CME (orange line) caused by a jet in the lower active region, the streamer is inflated due to the CME-driven shock (green line), which also perturbs the magnetic loop geometry toward the observer. The rotation of the loop means that the frequency dependence of the observed spike sources is masked. Throughout the remaining observation window, repeated magnetic reconnection occurs, accelerating electron beams along the loop direction, leading to an increased number of spike sources. In the post-CME phase, the magnetic field restores itself toward it's original configuration, such that the observed emission at the same frequency appears at larger sky-plane heights over time, moving across the sky plane at a velocity of 90 km s^{-1} between t_1 and t_2. The imaged sources are observed to drift along the direction of the magnetic field due to anisotropic radio-wave scattering, such that their centroids (black crosses) drift upward in the sky plane over time at fixed frequencies. The inset in the lower left panel shows counterpropagating electron beams induced by magnetic reconnection that can then produce the bidirectional Type IIIb. The streamer and shock front are not shown in the lower panels, and the smaller loops connected to the lower active region are excluded from the line-of-sight plane for clarity.

subsequent electron beam acceleration produces a greater number of spikes than in the pre-CME case. As the field restores itself toward its original configuration, a sky-plane drift of the imaged emission source locations is observed at a speed of $90 \, \mathrm{km \, s^{-1}}$. The distance from the acceleration region and location where the source begins to emit will depend on the beam density, velocity, and turbulence that determine the spatial location of Langmuir-wave growth. The emission quickly undergoes radio-wave scattering, with the strongest scattering power perpendicular to the field lines at a given location, such that the likely direction of photon propagation is parallel to the field, where the scattering power is weakest. This direction changes over time and distance due to the field geometry. The observed centroids are then displaced along the loop direction at fixed frequencies over time and expanded in area, and the true source location is never observed.

We observed spikes spread across many frequencies, implying that the acceleration heights may vary, or that the electron beams have differing initial densities and spatial sizes that can increase the onset time and burst starting frequencies (Reid et al. 2011; Reid & Kontar 2018b). The former agrees with the interpretation of spikes arising from many small sites of magnetic reconnection (Benz et al. 1982; Benz 1985), which may have been triggered by the CME. The frequency at which a spike is observed could then be an interplay between the acceleration location, the initial beam properties, and the coronal turbulence that will promote Langmuir-wave growth at a specific region of space.

6.4. Radio-wave Scattering Dominance

The scatter-dominated characteristics of spikes (source size and decay time) present power-law trends between decameter and decimeter observations. At 30 MHz, our estimation of the intrinsic source size suggests $l < 2r_n \Delta f / f \approx 1$ arcsec, where $\Delta f / f \sim 2 \times 10^{-3}$. Following the same approach at 333 MHz, Krucker et al. (1995) note a similar intrinsic size of $2''$ using a density scale height of 10^{10} cm. The similarity of the spike duration and plasma collision time has led to previous suggestions that this damping mechanism is the dominant factor controlling their short time profiles (McKim Malville et al. 1967; Tarnstrom & Philip 1972a; Benz 1986; Melnik et al. 2014). Using the collision time to infer the coronal temperature gives a range between 0.5–8.0 MK from 25 MHz to 1.4 GHz. However, due to significant broadening, the inferred temperatures would be reduced. At 30 MHz, typical decay times from simulations are ~ 0.2 s for $\alpha = 0.2$ (Kontar et al. 2019), reducing the median observed decay time in this study to 0.1 s and the coronal temperature to < 0.25 MK, which is much lower than expected above an active region. Figure 11 presents a $1/f$ trend for the spike decay times, with a similar power-law index to that for Type III bursts (Kontar et al. 2019). In addition, we show the inhomogeneity time τ_{inh}, which is the characteristic time for Langmuir waves to drift in velocity space (Kontar 2001), and can match the observed $1/f$ trend for the given input parameters, as described in Section 5.2. We see that varying the value of $\delta n_e / n_e$ can explain the spread in the observed data, where larger fluctuation amplitudes cause the Langmuir waves to drift faster in velocity space, resulting in shorter decay times—and indeed, $\delta n_e / n_e$ would be expected to vary from event to event. However, the trend required to match the observations with frequency is found from the inhomogeneity length scale λ, which increases linearly with r—we

estimate this to range from $2 - 100$ km between 1.03 and 2 $R_\odot$. The inhomogeneity time is also similar to the scattering-induced decay time from simulations (gray region in Figure 11), which is dictated by the density fluctuations. Since the observed time profile is a combination of both the intrinsic duration and broadening due to scattering as $\tau = (\tau_{\mathrm{source}}^2 + \tau_{\mathrm{scat}}^2)^{1/2}$, if $\tau_{\mathrm{source}} \ll \tau_{\mathrm{scat}}$ as the observations suggest, then radio-wave scattering is the dominant contribution and governs the observed decay time.

6.5. Magnetic Field Strength

The spread in $\Delta f / f$ can be predicted via the Langmuir-wave dispersion relation (Figure 12), which is significantly modified near 400 MHz through variation of the magnetic field strength, which could vary substantially between events. We note that we do not describe the theoretical spectral shape of spikes produced via plasma emission with this relation, which remains an open question that is beyond the scope of this study. For a fixed angle between the plasma wave and magnetic field of $\psi = 23°$ matching the average trend of the low-frequency spikes (where a range of ψ from $19°$ and $28°$ encompasses the low-frequency spike bandwidth ratios), the data suggest that between 0.4 and 3.5 GHz, the magnetic field strength between events could vary from 30 to 800 G. In the decameter range, spikes observed between 20 and 70 MHz (1.45–2.0 $R_\odot$ for the density model considered), the magnetic field strength varies between 1.2 and 3.5 G, larger than the model above active regions by Dulk & McLean (1978) of 0.5–1.65 G, but this model is derived from a compilation of different techniques where the data have a spread within a factor of three. This suggests that decameter spike events are associated with active regions that have stronger magnetic fields than average by a factor of ~ 2.

7. Conclusion

Solar radio spikes and Type IIIb bursts are observed to be associated with a trans-equatorial closed loop system, and could be associated with repeated magnetic reconnection in numerous small sites triggered by a streamer-puff CME. The typical observed bandwidth ratios suggest that the size of the emitting region is smaller than $1''$, which evolves in position over several tens of minutes owing to a perturbed magnetic geometry caused by the CME and shock propagation. Spikes and striae that are close in time and frequency have 90% intensity contours that almost completely overlap, suggesting that the sources emit radio waves from the same region of space. The emitting location will be determined by an interplay of the electron beam acceleration site, the beam characteristics, and the turbulent conditions. Fixed-frequency imaging of both burst types reveals strongly directive, superluminal centroid motion along the guiding magnetic field parallel to the solar limb, consistent with radio-wave scattering in an anisotropic medium. The observed spread in centroid velocity could be due to varying anisotropy, turbulence level, and emission angle within the loop. The strong scattering environment means that the emitting source locations do not correspond to the locations of the observed sources—from the Type IIIb frequency drift, the beam trajectory is likely associated with a region of the loop closer to the Sun along the ascending leg where the field trajectory is closer to the radial direction. Consequently, the region of acceleration and emission could be near the CME

flank. The frequency dependence of scattering-dominated properties from decameter to decimeter wavelengths present a consistent $1/f$ trend that is similar but not identical to that for Type III bursts (Kontar et al. 2019), suggesting that radio-wave scattering is significant in both domains and governs the observed decay and sizes. When we assume plasma emission, the observed spike bandwidth ratios can be replicated via the Langmuir-wave dispersion relation for conditions where $f_{ce} \ll f_{pe}$, with an order-of-magnitude increase above 400 MHz caused by the strong variation in magnetic field strength between the events at this scale. However, ECM emission cannot be discarded as the mechanism for spikes at gigahertz frequencies. In the decameter range, spike observations suggest that the magnetic field strength is stronger than average above active regions by a factor of ~2.

Appendix
Spike Characteristics with Frequency

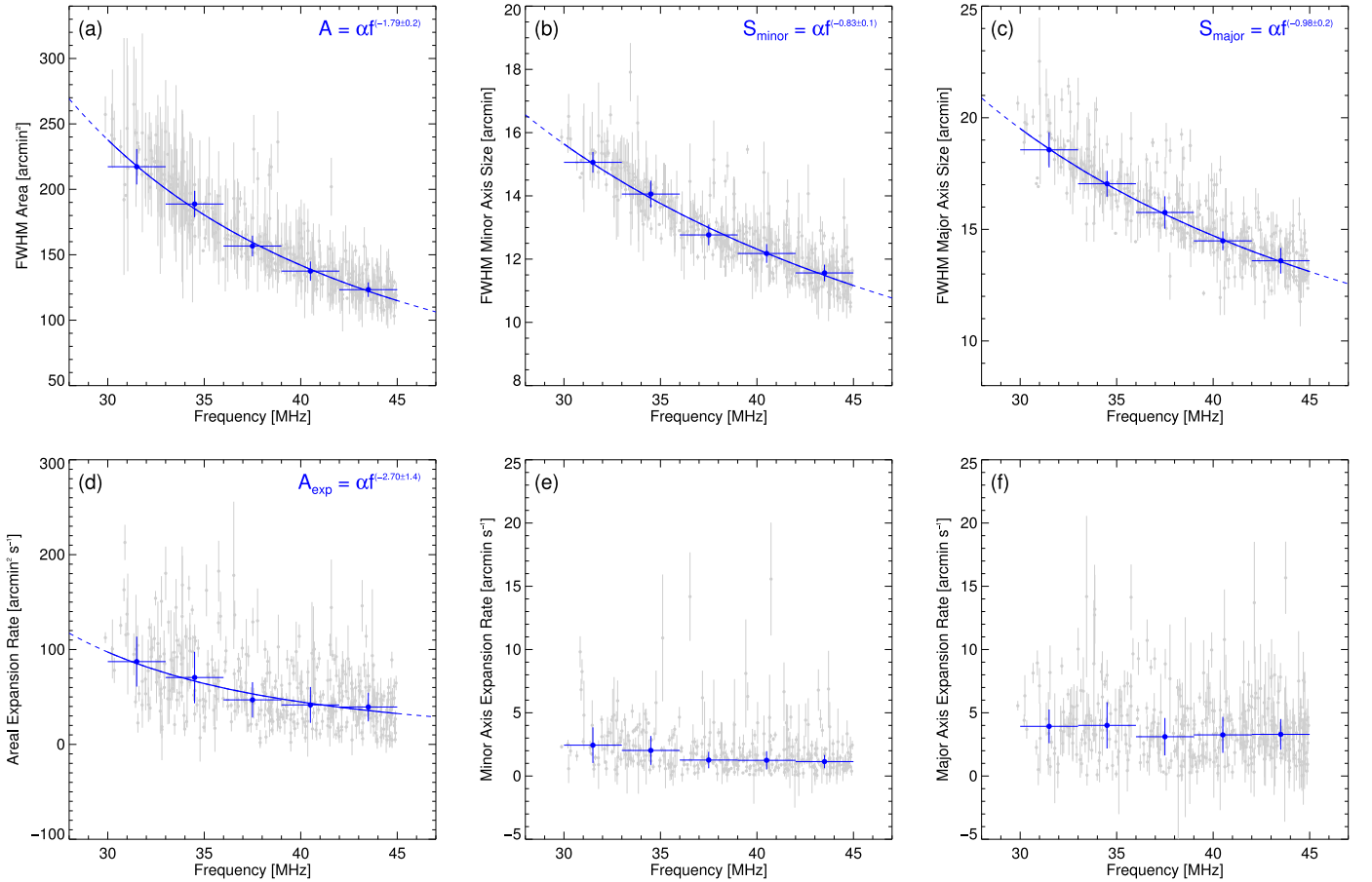Figures A1 and A2 present the full set of spike characteristics from imaging and dynamic spectra, respectively.

Figure A1. Spike characteristics derived from imaging observations. The gray data show the observed quantity and associated uncertainties. The blue points show the median values across 3 MHz bins, with the vertical error as the interquartile range between the 25th and 75th percentiles, and a power-law fit given by the solid blue line. Panel (a) Observed FWHM area. Panel (b) FWHM minor axis size. Panel (c) FWHM major axis size. Panel (d) Areal expansion rate. Panel (e) Minor axis expansion rate. Panel (f) Major axis expansion rate.
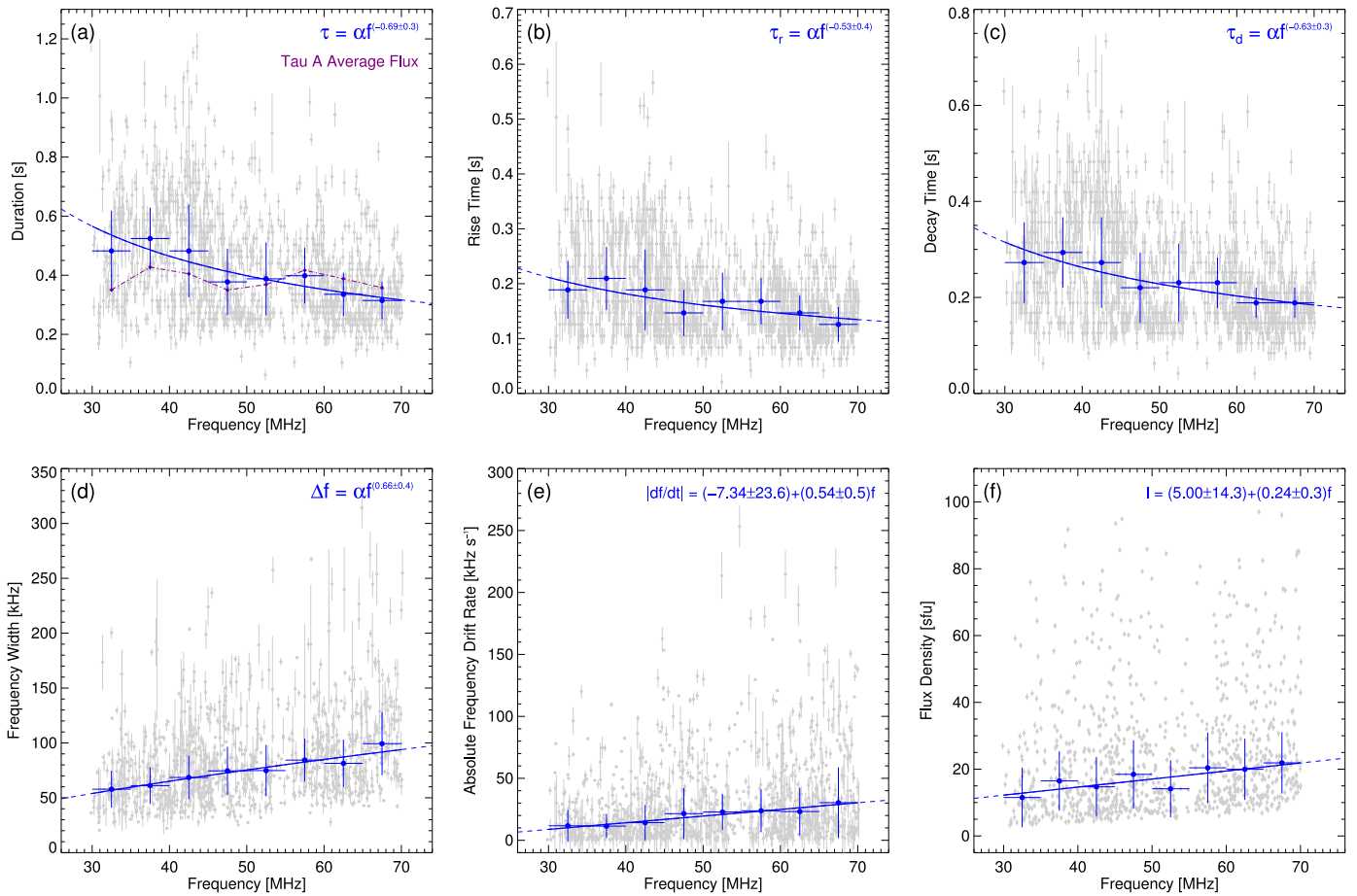
Figure A2. Spike characteristics derived from dynamic spectra observations. The light gray points show the data with associated uncertainties. The blue points show the median values across 5 MHz bins, with the vertical error as the interquartile range representing the 25th and 75th percentiles, and a power-law or linear fit shown by the blue line. Panel (a) FWHM duration. The purple points show the median Tau A flux on the day of observation. Panel (b) Rise time at the half-maximum intensity level. Panel (c) Decay time at the half-maximum intensity level. Panel (d) FWHM bandwidth. Panel (e) Absolute frequency drift rate. Panel (f) Flux at the light-curve peak.

ORCID iDs

Daniel L. Clarkson https://orcid.org/0000-0003-1967-5078
Eduard P. Kontar https://orcid.org/0000-0002-8078-0902
Nicole Vilmer https://orcid.org/0000-0002-6872-3630
Mykola Gordovskyy https://orcid.org/0000-0003-2291-4922
Xingyao Chen https://orcid.org/0000-0002-1810-6706
Nicolina Chrysaphi https://orcid.org/0000-0002-4389-5540

References

Altyntsev, A. T., Grechnev, V. V., Konovalov, S. K., et al. 1996, ApJ, 469, 976
Altyntsev, A. T., Grechnev, V. V., Zubkova, G. N., et al. 1995, A&A, 303, 249
Aschwanden, M. J., Benz, A. O., Dennis, B. R., & Schwartz, R. A. 1995, ApJ, 455, 347
Aschwanden, M. J., Newmark, J. S., Delaboudinière, J.-P., et al. 1999, ApJ, 515, 842
Barrow, C. H., Zarka, P., & Aubier, M. G. 1994, A&A, 286, 597
Battaglia, M., & Kontar, E. P. 2012, ApJ, 760, 142
Battaglia, M., Sharma, R., Luo, Y., et al. 2021, ApJ, 922, 134
Bemporad, A., Sterling, A. C., Moore, R. L., & Poletto, G. 2005, ApJL, 635, L189
Benz, A. O. 1985, SoPh, 96, 357
Benz, A. O. 1986, SoPh, 104, 99
Benz, A. O., Csillaghy, A., & Aschwanden, M. J. 1996, A&A, 309, 291
Benz, A. O., Jaeggi, M., & Zlobec, P. 1982, A&A, 109, 305
Benz, A. O., Saint-Hilaire, P., & Vilmer, N. 2002, A&A, 383, 678
Benz, A. O., Su, H., Magun, A., & Stehling, W. 1992, A&AS, 93, 539

Chen, X., Kontar, E. P., Chrysaphi, N., et al. 2020, ApJ, 905, 43
Chen, X., Kontar, E. P., Yu, S., et al. 2018, ApJ, 856, 73
Chernov, G. P. 1977, SvA, 21, 612
Chernov, G. P. 2011, Fine Structure of Solar Radio Bursts, Vol. 375 (Berlin: Springer)
Chrysaphi, N., Reid, H. A. S., & Kontar, E. P. 2020, ApJ, 893, 115
Clarkson, D. L., Kontar, E. P., Gordovskyy, M., Chrysaphi, N., & Vilmer, N. 2021, ApJL, 917, L32
Cliver, E. W., White, S. M., & Balasubramaniam, K. S. 2011, ApJ, 743, 145
Csillaghy, A., & Benz, A. O. 1993, A&A, 274, 487
Dąbrowski, B. P., Rudawy, P., & Karlický, M. 2011, SoPh, 273, 377
Dulk, G. A., & McLean, D. J. 1978, SoPh, 57, 279
Fleishman, G. D., & Mel'nikov, V. F. 1998, PhyU, 41, 1157
Gary, D. E., Hurford, G. J., & Flees, D. J. 1991, ApJ, 369, 255
Gary, G. A. 2001, SoPh, 203, 71
Gordovskyy, M., Kontar, E. P., Clarkson, D. L., Chrysaphi, N., & Browning, P. K. 2022, ApJ, 925, 140
Guedel, M., & Benz, A. O. 1990, A&A, 231, 202
Holman, G. D., Aschwanden, M. J., Aurass, H., et al. 2011, SSRv, 159, 107
Jeffrey, N. L. S., & Kontar, E. P. 2011, A&A, 536, A93
Khan, J. I., & Aurass, H. 2006, A&A, 457, 319
Kontar, E. P. 2001, A&A, 375, 629
Kontar, E. P., Chen, X., Chrysaphi, N., et al. 2019, ApJ, 884, 122
Kontar, E. P., Hannah, I. G., & MacKinnon, A. L. 2008, A&A, 489, L57
Kontar, E. P., Perez, J. E., Harra, L. K., et al. 2017a, PhRvL, 118, 155101
Kontar, E. P., Yu, S., Kuznetsov, A. A., et al. 2017b, NatCo, 8, 1515
Krucker, S., Aschwanden, M. J., Bastian, T. S., & Benz, A. O. 1995, A&A, 302, 551
Krucker, S., Benz, A. O., & Aschwanden, M. J. 1997, A&A, 317, 569
Kuznetsov, A. A., Chrysaphi, N., Kontar, E. P., & Motorina, G. 2020, ApJ, 898, 94

Kuznetsov, A. A., & Kontar, E. P. 2019, A&A, 631, L7

Markeev, A. K., & Chernov, G. P. 1971, SvA, 14, 835

McKim Malville, J., Aller, H. D., & Jensen, C. J. 1967, ApJ, 147, 711

Melnik, V. N., Shevchuk, N. V., Konovalenko, A. A., et al. 2014, SoPh, 289, 1701

Melrose, D. B. 1985, in Solar Radiophysics: Studies of Emission from the Sun at Metre Wavelengths, ed. D. J. McLean & N. R. Labrum (Cambridge: Cambridge Univ. Press), 177

Melrose, D. B., & Dulk, G. A. 1982, ApJ, 259, 844

Messmer, P., & Benz, A. O. 2000, A&A, 354, 287

Mészárosová, H., Veronig, A., Zlobec, P., & Karlický, M. 2003, A&A, 407, 1115

Musset, S., Maksimovic, M., Kontar, E., et al. 2021, A&A, 656, A34

Nita, G. M., Fleishman, G. D., & Gary, D. E. 2008, ApJ, 689, 545

Paesold, G., Benz, A. O., Klein, K. L., & Vilmer, N. 2001, A&A, 371, 333

Pécseli, H. 2012, Waves and Oscillations in Plasmas (Boca Raton, FL: CRC Press)

Reid, H. A. S., & Kontar, E. P. 2017, A&A, 606, A141

Reid, H. A. S., & Kontar, E. P. 2018a, A&A, 614, A69

Reid, H. A. S., & Kontar, E. P. 2018b, ApJ, 867, 158

Reid, H. A. S., Vilmer, N., & Kontar, E. P. 2011, A&A, 529, A66

Rozhansky, I. V., Fleishman, G. D., & Huang, G. L. 2008, ApJ, 681, 1688

Sharykin, I. N., Kontar, E. P., & Kuznetsov, A. A. 2018, SoPh, 293, 115

Shevchuk, N. V., Melnik, V. N., Poedts, S., et al. 2016, SoPh, 291, 211

Staehli, M., & Magun, A. 1986, SoPh, 104, 117

Tan, B., Chen, N., Yang, Y.-H., et al. 2019, ApJ, 885, 90

Tan, B. L., Karlický, M., Mészárosová, H., et al. 2016, SoPh, 291, 2407

Tarnstrom, G. L., & Philip, K. W. 1972a, A&A, 17, 267

Tarnstrom, G. L., & Philip, K. W. 1972b, A&A, 16, 21

van Haarlem, M. P., Wise, M. W., Gunst, A. W., et al. 2013, A&A, 556, A2

Wang, M., Fu, Q. J., Xie, R. X., & Huang, G. L. 1999, SoPh, 189, 331

Wang, S. J., Yan, Y. H., & Fu, Q. J. 2002, SoPh, 209, 185

Wang, S. J., Yan, Y. H., Liu, Y. Y., et al. 2008, SoPh, 253, 133

Zaitsev, V. V. 1975, SvA, 18, 475

Zhang, P., Zucca, P., Sridhar, S. S., et al. 2020, A&A, 639, A115

Zhelezniakov, V. V., & Zaitsev, V. V. 1975, A&A, 39, 107